Supporting Information

Defect-derived Catalytic Sites in Ce/Zr-UiO-66 for Degradation of Hexachlorobenzene

Zhengyan Wang[a], Chenhao Yuan[a], Dong Yang[a], Mifen Cui[a], Jihai Tang[a], Zhuxiu Zhang[a,*] and Xu Qiao[a,*]

[a]*State Key Laboratory of Materials-Oriented Chemical Engineering, College of Chemical Engineering, Nanjing Tech University, No. 30 Puzhunan Road, Nanjing 211816, China*

**Corresponding author. Tel.: +86 25 83587168; E-mail: zhuxiu.zhang@njtech.edu.cn*

**Corresponding author. Tel.: +86 25 83172298; E-mail: qct@njtech.edu.cn*

Table of Contents

S1 The number of formate ligands on the clusters of Ce/Zr-UiO-66-FA post-treatment at different temperatures.

Table S1. The number of formate ligands on the Ce/Zr-UiO-66-FA-P clusters after post-treatment at different temperatures.

Samples	After post-treatment number of formate ligands per cluster
Ce/Zr-UiO-66-FA-P-80℃	1.55
Ce/Zr-UiO-66-FA-P-120℃	0.43
Ce/Zr-UiO-66-FA-P-150℃	0.00
Ce/Zr-UiO-66-FA-P-200℃	0.00
Ce/Zr-UiO-66-FA-P-250℃	0.00

S2 IR Spectra with Ce/Zr-UiO-66-FA at high temperature in N_2

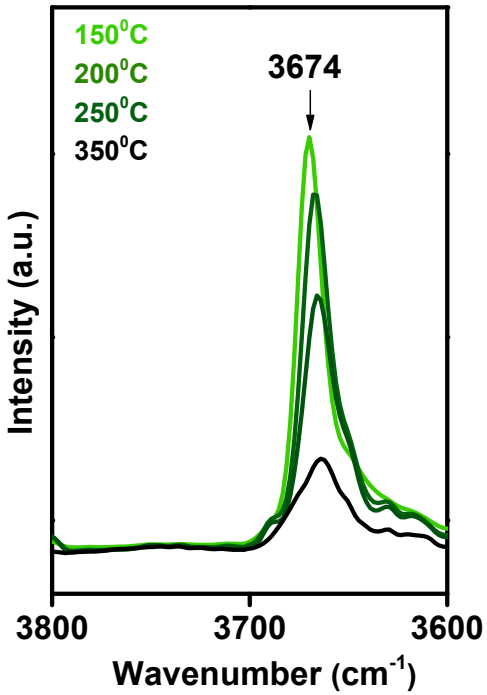

Figure S1. IR spectra in the hydroxyl-group region characterizing Ce/Zr-UiO-66-FA in flowing N_2 as the temperature was ramped from 150 to 350 °C.

S3 TGA curves of Ce/Zr-UiO-66-FA and Ce/Zr-UiO-66-FA-P

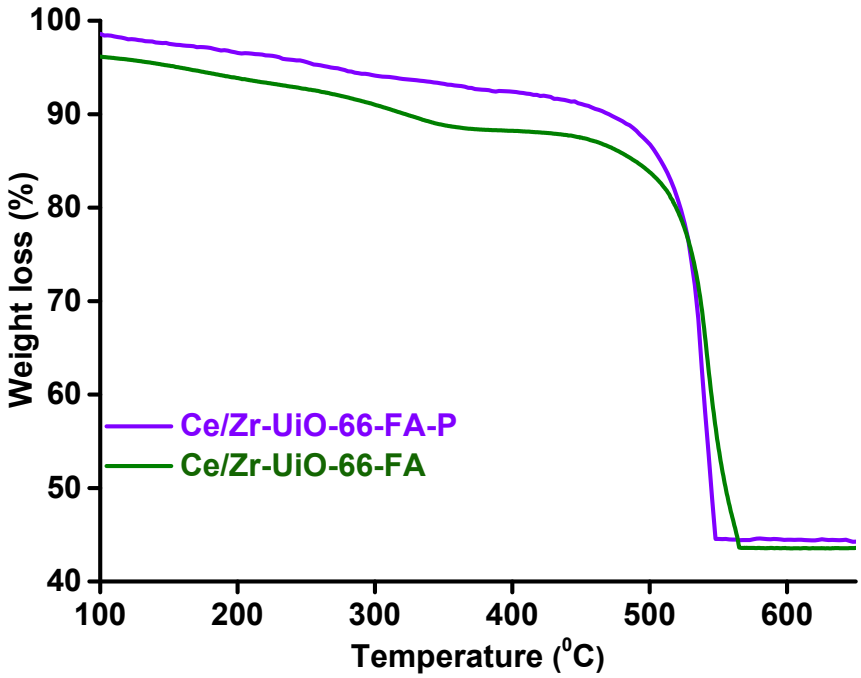

Figure S2. TGA curves of Ce/Zr-UiO-66-FA and Ce/Zr-UiO-66-FA-P.

S4 Reproducibility Tests of post-treatment over Ce/Zr-UiO-66-FA

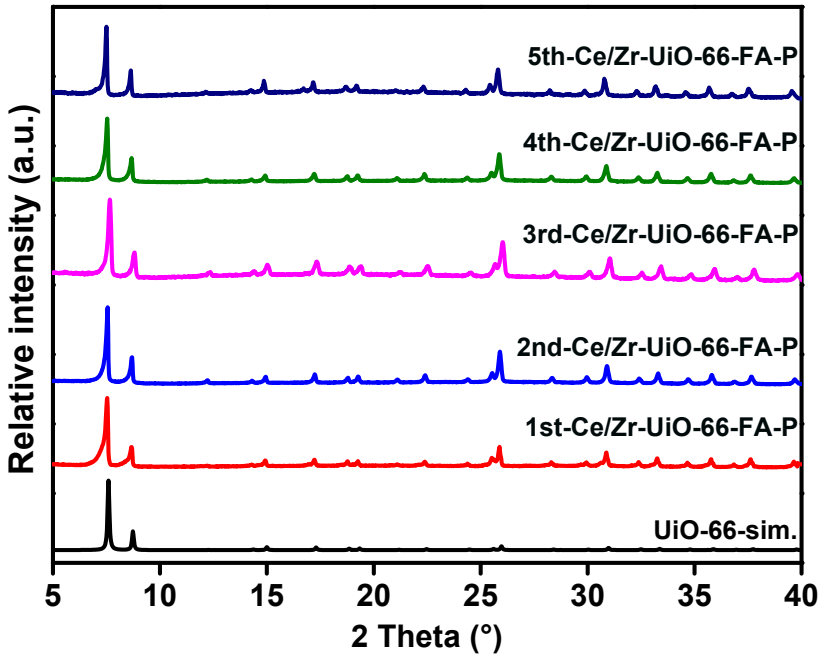

Figure S3. PXRD patterns of Ce/Zr-UiO-66-FA-P

Table S2. BET surface area and number of ligands per metal cluster for Ce/Zr-UiO-66-FA-P.

Samples	BET surface area (m^2/g)	Number of ligands per cluster
1st-Ce/Zr-UiO-66-FA-P	1349	0.00
2nd-Ce/Zr-UiO-66-FA-P	1357	0.00
3rd-Ce/Zr-UiO-66-FA-P	1350	0.00
4th-Ce/Zr-UiO-66-FA-P	1345	0.00
5th-Ce/Zr-UiO-66-FA-P	1352	0.00

S5 Characterization of Ce/Zr-UiO-66, Ce/Zr-UiO-66 MeOH treatment and Ce/Zr-UiO-66-P

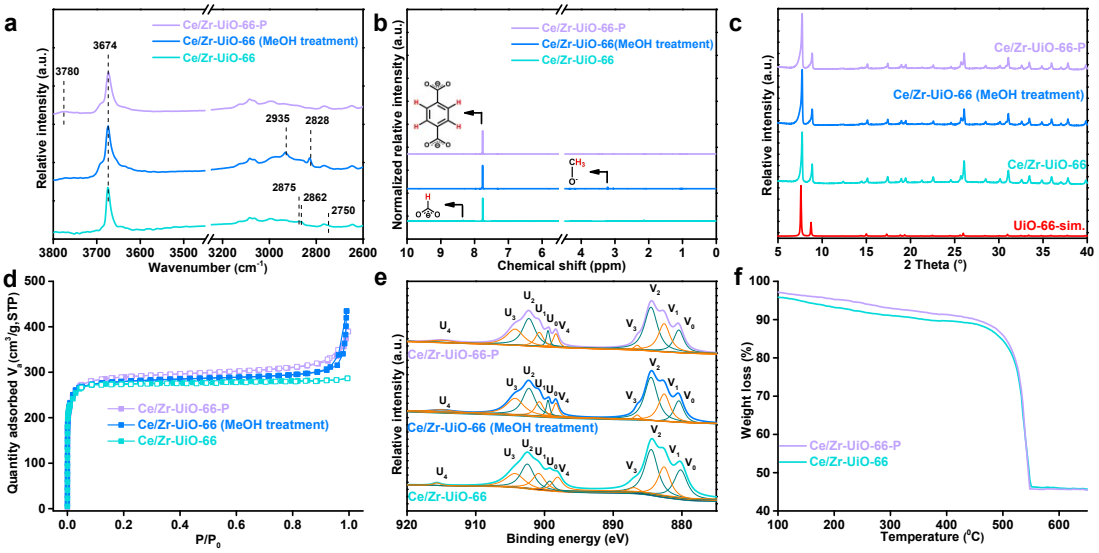

Figure S4. (A) FT-IR spectra, (B) ^{1}H NMR, (C) PXRD patterns, (D) Nitrogen adsorption and desorption isotherms, (E) Ce 3d XPS spectra of Ce/Zr-UiO-66, Ce/Zr-UiO-66 (MeOH treatment) and Ce/Zr-UiO-66-P; (F) TGA curves of Ce/Zr-UiO-66 and Ce/Zr-UiO-66-P.

Table S3. BET surface area, number of formate/methoxy ligands per metal cluster and Ce content for Ce/Zr-UiO-66, Ce/Zr-UiO-66 (MeOH treatment) and Ce/Zr-UiO-66-P.

Samples	BET surface area (m^2/g)	Number of formate ligands per cluster	Number of methoxy ligands per cluster	Ce (wt%)
Ce/Zr-UiO-66	981	0.19	-	4.07
Ce/Zr-UiO-66 (MeOH treatment)	988	0.00	0.19	4.07
Ce/Zr-UiO-66-P	995	0.00	0.00	4.08

Based on Figure S4 and Table S3, it is shown that the structural changes of the post-treatment material Ce/Zr-UiO-66-P was consistent with Ce/Zr-UiO-66-FA-P, with no change in crystal structure and BET surface area. In the Ce/Zr-UiO-66-P, the valence state of Ce atoms presented a mixed valence state of Ce(III) and Ce(IV). The complete substitution of formate ligands on the cluster of Ce/Zr-UiO-66-P with terminal hydroxyl groups was demonstrated by ^{1}H NMR and FT-IR.

S6 Pore size distributions for Ce/Zr-UiO-66-P and Ce/Zr-UiO-66-FA-P.

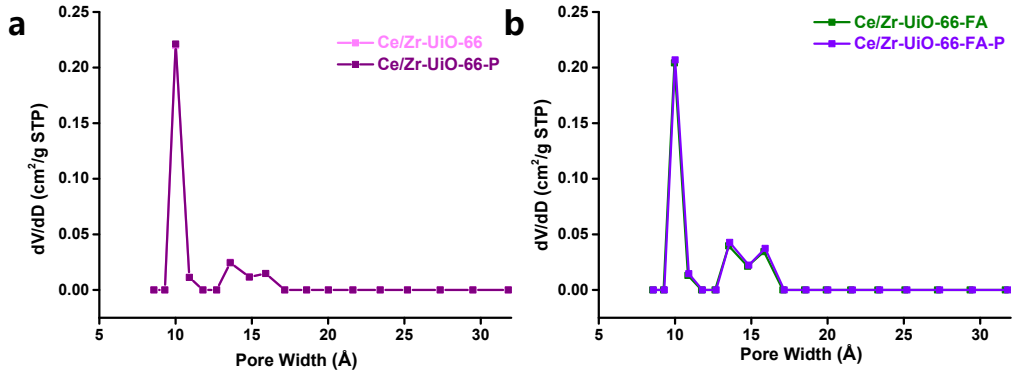

Figure S5. Pore size distributions calculated by DFT method for (a) Ce/Zr-UiO-66 and Ce/Zr-UiO-66-P; (b) Ce/Zr-UiO-66-FA and Ce/Zr-UiO-66-FA-P.

Table S4. Pore volume of Ce/Zr-UiO-66-P and Ce/Zr-UiO-66-FA-P calculated by DFT method

Samples	Pore Volume (cm^3/g)
Ce/Zr-UiO-66	0.52
Ce/Zr-UiO-66-P	0.52
Ce/Zr-UiO-66-FA	0.63
Ce/Zr-UiO-66-FA-P	0.64

S7 SEM Images of Ce/Zr-UiO-66-P and Ce/Zr-UiO-66-FA-P

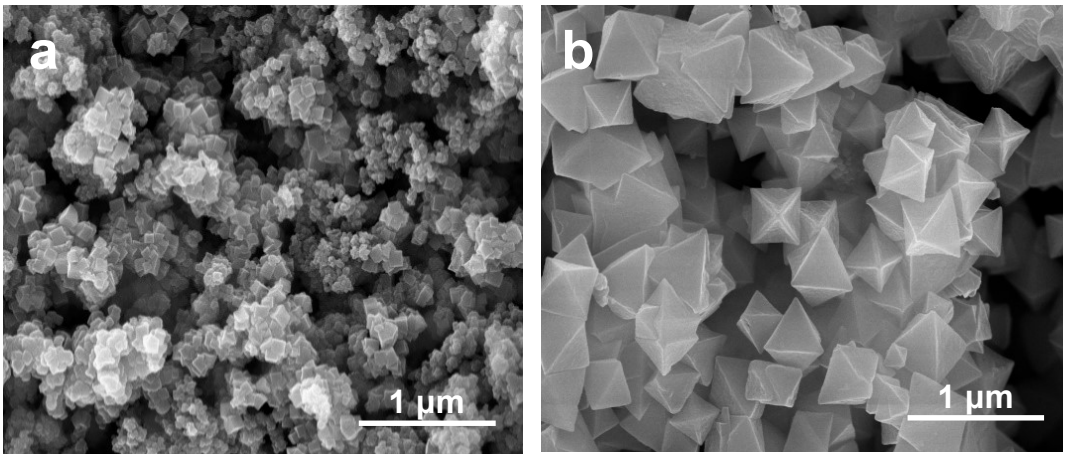

Figure S6. SEM images of (A) Ce/Zr-UiO-66-P and (B) Ce/Zr-UiO-66-FA-P.

S8 HR-TEM image and EDS spectra of Ce/Zr-UiO-66-FA and Ce/Zr-UiO-66-FA-P.

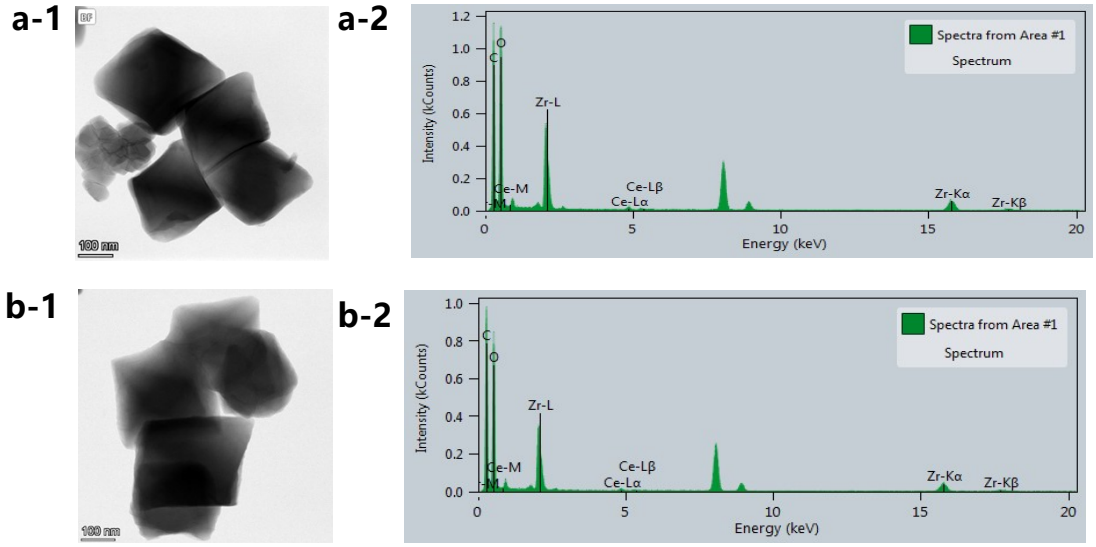

Figure S7. HR-TEM image (a-1) and EDS spectra (a-2) of Ce/Zr-UiO-66-FA; (b) HAADF-STEM image (b-1) and EDS spectra (a-2) of Ce/Zr-UiO-66-FA-P.

S9 HAADF-STEM image and EDS element mapping of Ce/Zr-UiO-66-FA and Ce/Zr-UiO-66-FA-P.

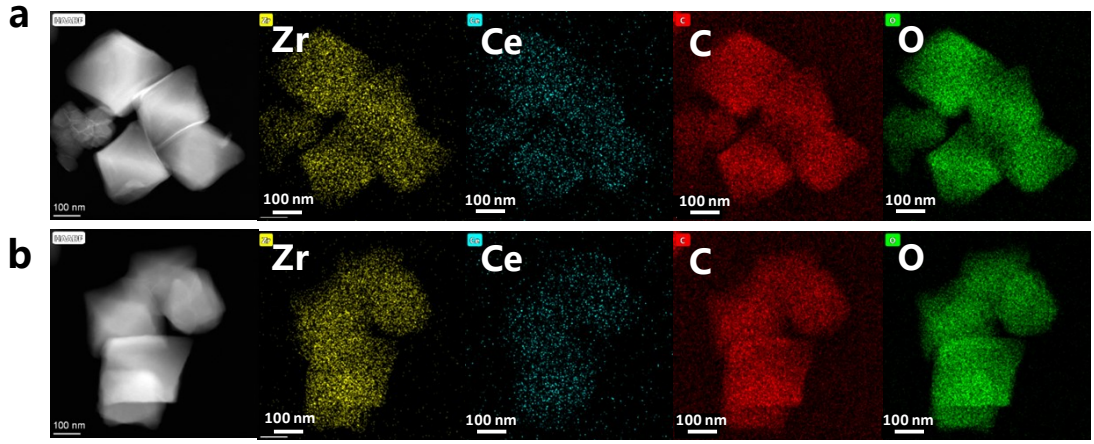

Figure S8. (a) HAADF-STEM image and EDS element mapping of Ce/Zr-UiO-66-FA; (b) HAADF-STEM image and EDS element mapping of Ce/Zr-UiO-66-FA-P. (Zr atoms: yellow, Ce atoms: blue, C atoms: red, O atoms: green)

S10 Raman spectra of Zr-UiO-66, Ce/Zr-UiO-66-FA-P and Ce-UiO-66.

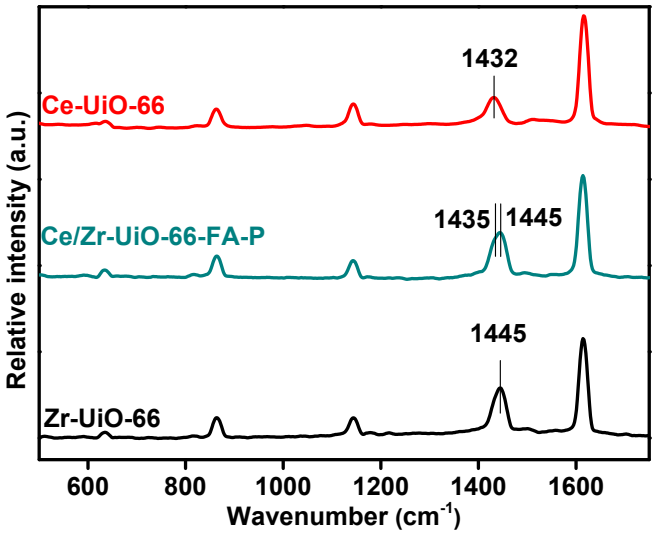

Figure S9. Raman spectra of Zr-UiO-66, Ce/Zr-UiO-66-FA-P and Ce-UiO-66

S11 H_2-TPR and Cyclic voltammetry of Ce/Zr-UiO-66-FA and Ce/Zr-UiO-66-FA-P.

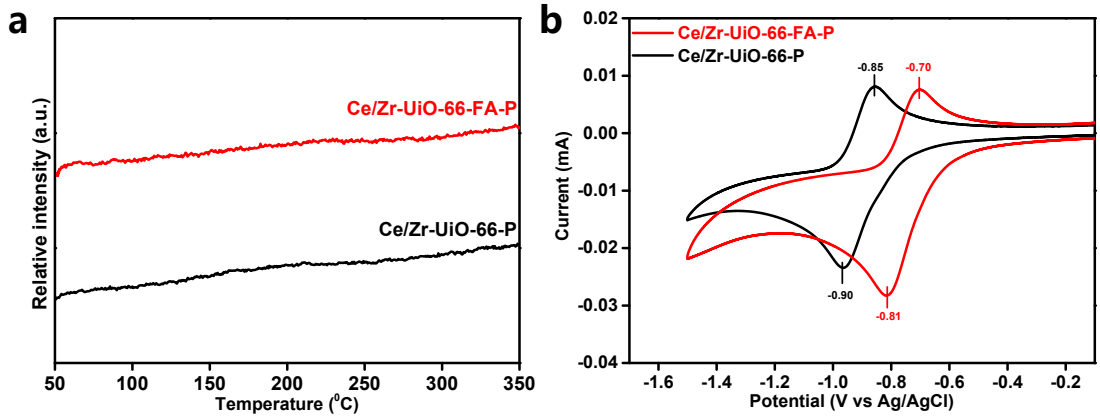

Figure S10. (a) H_2-TPR and (b) Cyclic voltammetry of the Ce/Zr-UiO-66-P and Ce/Zr-UiO-66-FA-P

Cyclic voltammetry test method

N-methylpyrrolidone (C_5H_9NO, purity 98%) and Polyvinylidene fluoride powder ($(CH_2CF_2)_n$, average Mw ~ 400,000) were purchased from Aladdin.

Preparation of electrode sheet: a titanium plate (2 cm × 3 cm × 1 mm) was washed with ultrapure water for 15 min. The ground samples (0.3 g), N-methylpyrrolidone (0.01g) and polyvinylidene fluoride (1 mL) were mixed and then stirred evenly. The surface of the titanium plate was evenly coated with a mixture of agents and then dried in an oven (120 ℃) for 120 min.

Cyclic voltammetry (CV) curve was measured by a three-electrode system. The glass carbon electrode (3 mm) served as the working electrode, the carbon as the counter electrode, and the reference electrode was the Ag wire. 0.1 M TBAP DMF was used as electrolyte. Electrocatalytic testing was performed at room temperature. The CV test parameters were: scanning speed = 0.1 V/s, initial potential =Eoc, and final potential = -1.5 V.

S12 The effect of different solvents on the catalytic degradation of HCB over Ce/Zr-UiO-66-FA-P

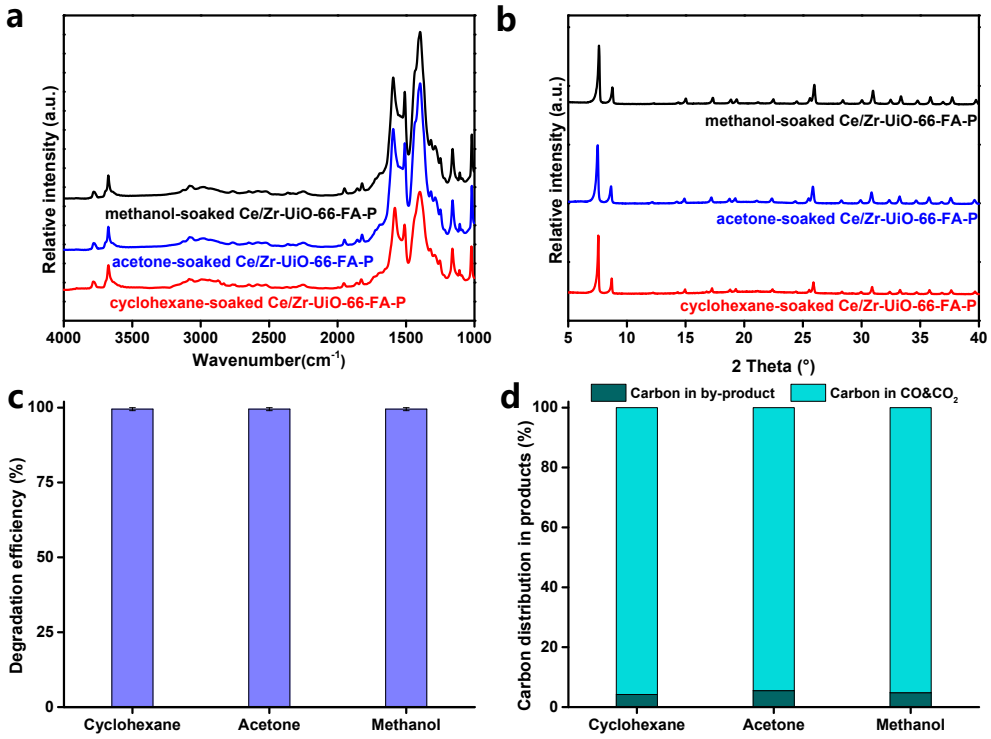

Figure S11. Cyclohexane-soaked Ce/Zr-UiO-66-FA-P, acetone-soaked Ce/Zr-UiO-66-FA-P and methanol-soaked Ce/Zr-UiO-66-FA-P of (a) after drying under high vacuum of FT-IR spectra; (b) after the reaction of the PXRD patterns; (c) Degradation efficiency and (d) Carbon distribution of the products for the catalytic degradation of HCB at 250 ℃;

Table S5 The kinetic constant and reaction rate for the catalytic degradation of HCB at 250 ℃ over cyclohexane-soaked Ce/Zr-UiO-66-FA-P, acetone-soaked Ce/Zr-UiO-66-FA-P and methanol-soaked Ce/Zr-UiO-66-FA-P

Samples	kinetic constant (k) (min^{-1})	reaction rate (mmol /(g*min))
cyclohexane-soaked Ce/Zr-UiO-66-FA-P	0.077	0.0054
acetone-soaked Ce/Zr-UiO-66-FA-P	0.075	0.0053
methanol-soaked Ce/Zr-UiO-66-FA-P	0.076	0.0054

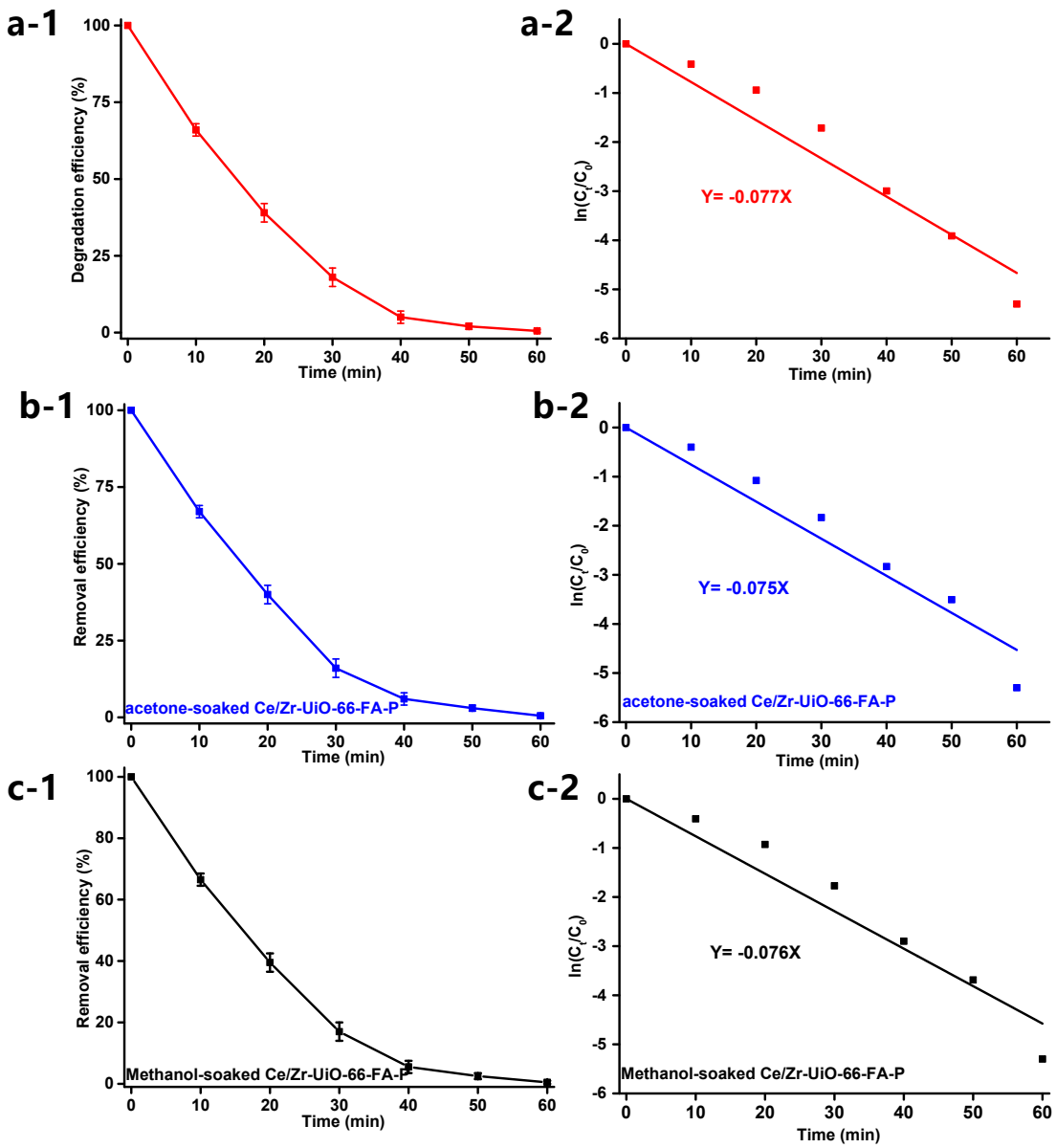

Figure S12. The removal efficiency for HCB at 250 ℃ in different time over cyclohexane-soaked Ce/Zr-UiO-66-FA-P (a-1), acetone-soaked Ce/Zr-UiO-66-FA-P (b-1) and methanol-soaked Ce/Zr-UiO-66-FA-P (c-1); The first order kinetics model of HCB degradation over cyclohexane-soaked Ce/Zr-UiO-66-FA-P (a-2), acetone-soaked Ce/Zr-UiO-66-FA-P (b-2) and methanol-soaked Ce/Zr-UiO-66-FA-P (c-2).

S13 The different the number of open metal sites in the Ce/Zr-UiO-66-FA-P metal clusters of the degradation efficiency and carbon distribution of the products in the catalytic degradation of HCB

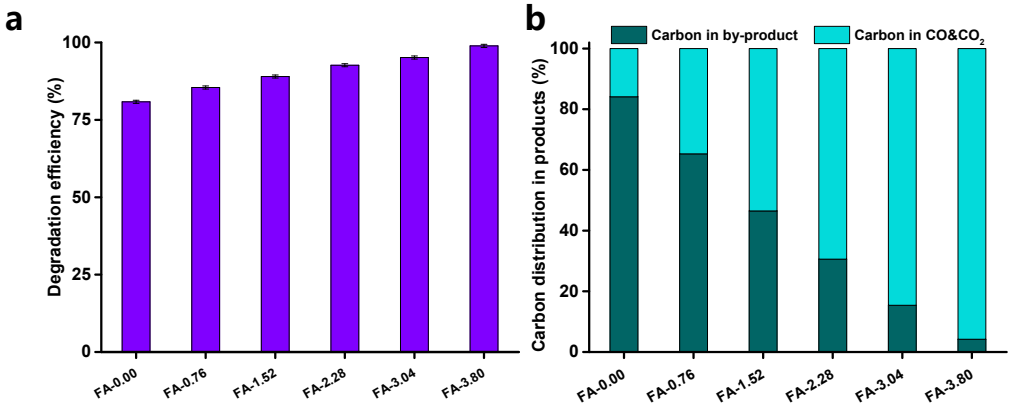

Figure S13. (a) Degradation efficiency of HCB at 150 ℃ and (b) carbon distribution of the products at 250 ℃ over the different number of open-metal sites on the Ce/Zr-UiO-66 metal clusters

Table S6. Number of formate ligands and after post-treatment per clusters for FA-0.00/0.76/1.52/2.28/3.04/3.80

Samples	Number of formate ligands per cluster	After post-treatment Number of formate ligands per cluster
FA-0.00	0.19	0.00
FA-0.76	1.45	0.00
FA-1.52	1.76	0.00
FA-2.28	2.10	0.00
FA-3.04	2.41	0.00
FA-3.80	2.69	0.00

S14 The effect of crystal size and the number of defects on the surface acidity and degradation efficiency for HCB.

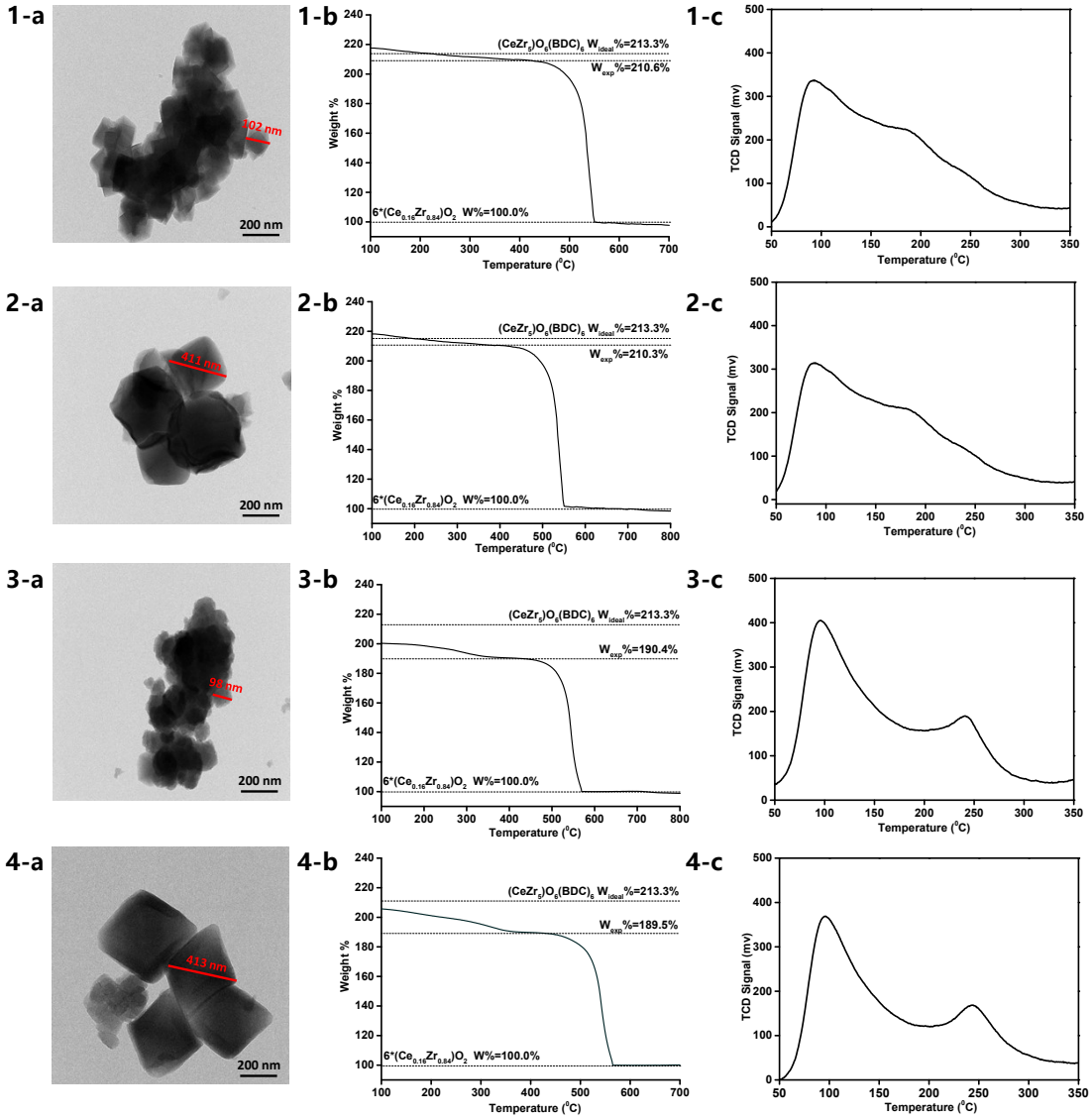

Figure S14. Ce/Zr-UiO-66-P-0.29, Ce/Zr-UiO-66-FA-P-0.32, Ce/Zr-UiO-66-P-2.49 and Ce/Zr-UiO-66-FA-P-2.52 of (a) TEM images; (b) TGA curve and (c) NH_3-TPD

Table S7. Crystal size, Number of missing linkers per cluster and Total amount of acidity of Ce/Zr-UiO-66-P-0.29, Ce/Zr-UiO-66-FA-P-0.32, Ce/Zr-UiO-66-P-2.43 and Ce/Zr-UiO-66-FA-P-2.52

Samples	Crystal size (nm)	Number of missing linkers per cluster	Total amount (mmol NH_3/g)
Ce/Zr-UiO-66-P-0.29	102	0.29	1.21
Ce/Zr-UiO-66-FA-P-0.32	411	0.32	1.17
Ce/Zr-UiO-66-P-2.43	98	2.43	3.83
Ce/Zr-UiO-66-FA-P-2.52	413	2.52	3.64

Synthesis of Ce/Zr-UiO-66-P-2.43: We mixed 100 mg of Ce/Zr-UiO-66-P with 30 ml DMF and 3.8 ml formic acid and heated it for 12 hours at 120°C. After washing with DMF and acetone, followed by 12 hours of high vacuum activation at 120°C and post-treatment with methanol and water vapor. In Fig. 4 and Table 3, its crystal size was 98 nm with 2.43 missing linkers per cluster..

Synthesis of Ce/Zr-UiO-66-FA-P-0.32: To construct Ce/Zr-UiO-66-FA-P with a large crystal size and little defect sites on the clusters, we mixed 100 mg of Ce/Zr-UiO-66-FA-P with 30 ml of DMF and 0.167g of H2BDC and heated it for 12 hours at 120°C. After washing with DMF and acetone, followed by 12 hours of high vacuum activation at 120°C and post-treatment with methanol and water vapor. In Fig. 4 and Table 3, its crystal size was 413 nm with 0.32 missing linkers per cluster.

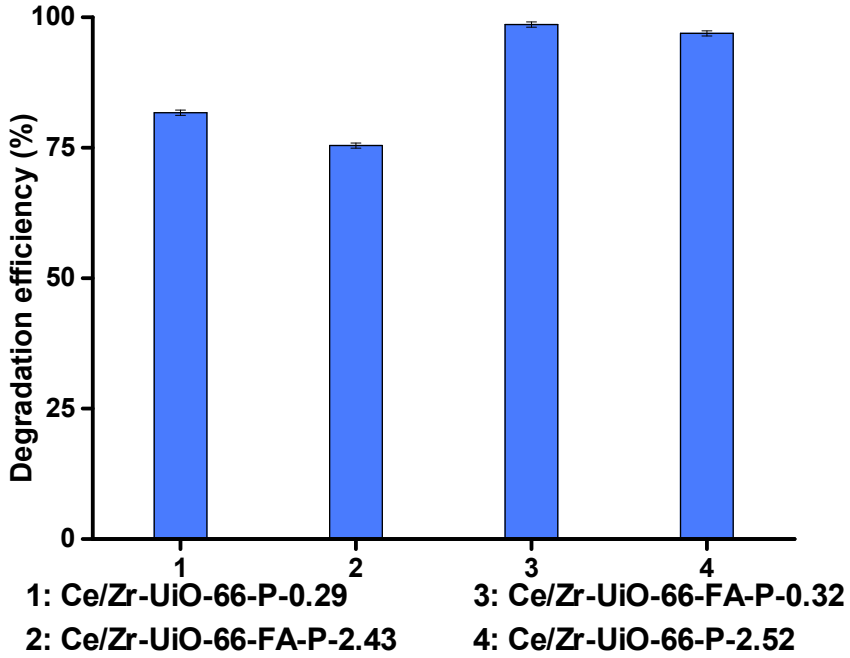

Figure S15. Degradation efficiency for HCB at 150 ℃ in 1h over Ce/Zr-UiO-66-P-0.29, Ce/Zr-UiO-66-FA-P-0.32, Ce/Zr-UiO-66-P-2.49 and Ce/Zr-UiO-66-FA-P-2.52

S15 The kinetic constants for the Zr-UiO-66, Ce/Zr-UiO-66-FA-P and Ce-UiO-66 in the catalytic degradation of HCB

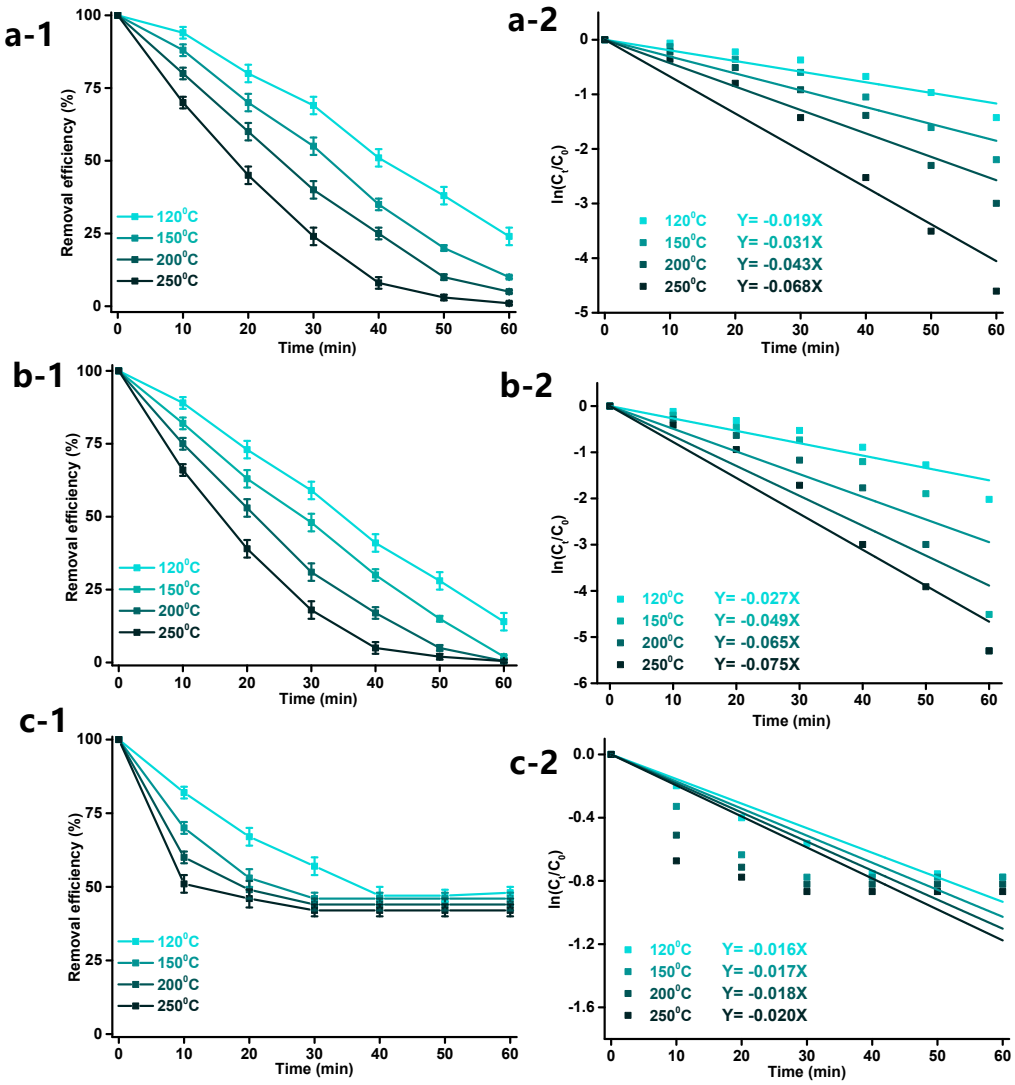

Figure S16. The removal efficiency for HCB at 120/150/200/250 ℃ in different time over Zr-UiO-66 (a-1), Ce/Zr-UiO-66-FA-P (b-1) and Ce-UiO-66 (c-1); The first order kinetics model of HCB degradation at 90/120/150/200/250 ℃ over Zr-UiO-66 (a-2), Ce/Zr-UiO-66-FA-P (b-2) and Ce-UiO-66 (c-2).

S16 The activation energies TON and TOF for Zr-UiO-66, Ce/Zr-UiO-66-FA-P, Ce-UiO-66, H_2BDC, $ZrCl_4$ and $Ce(NH_3)_2(NO_3)$ in the catalytic degradation of HCB

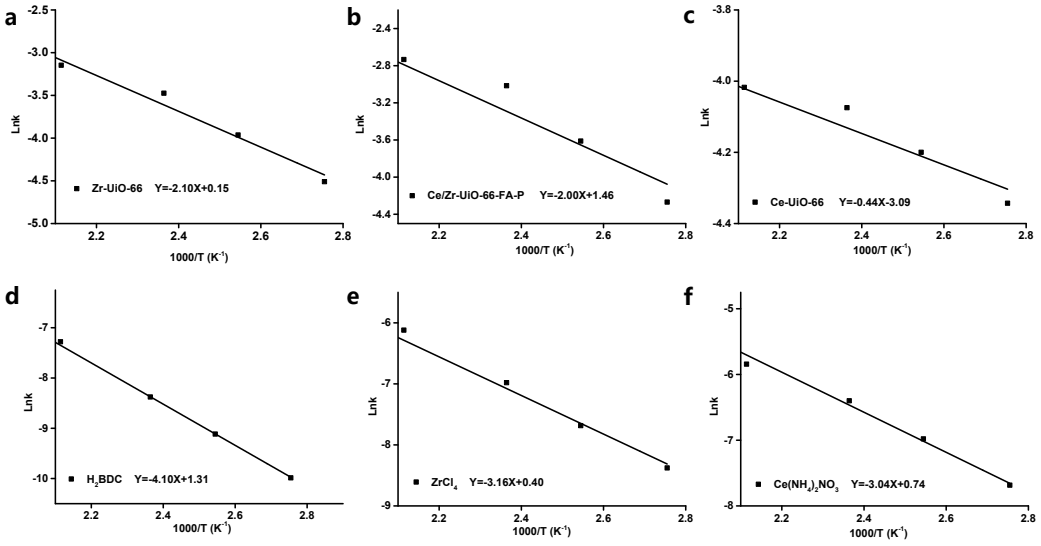

Figure S17. Arrhenius plots for the Zr-UiO-66 (a), Ce/Zr-UiO-66-FA-P (b) Ce-UiO-66 (c) H_2BDC (d), $ZrCl_4$ (e) and $Ce(NH_4)_2NO_3$ (f) in the catalytic degradation of HCB.

Table S8. The TON and TOF for the catalytic degradation of HCB over Zr-UiO-66, Ce/Zr-UiO-66-FA-P, Ce-UiO-66, H_2BDC, $ZrCl_4$ and $Ce(NH_3)_2(NO_3)$

Samples	TON	TOF
Zr-UiO-66	0.36	0.0060
Ce/Zr-UiO-66-FA-P	0.39	0.0065
Ce-UiO-66	0.22	0.0037
H_2BDC	0.053	0.00088
$ZrCl_4$	0.12	0.0019
$Ce(NH_3)_2NO_3$	0.15	0.0024

S17 PXRD pattern of $Ce_xZr_{1-x}O_2$

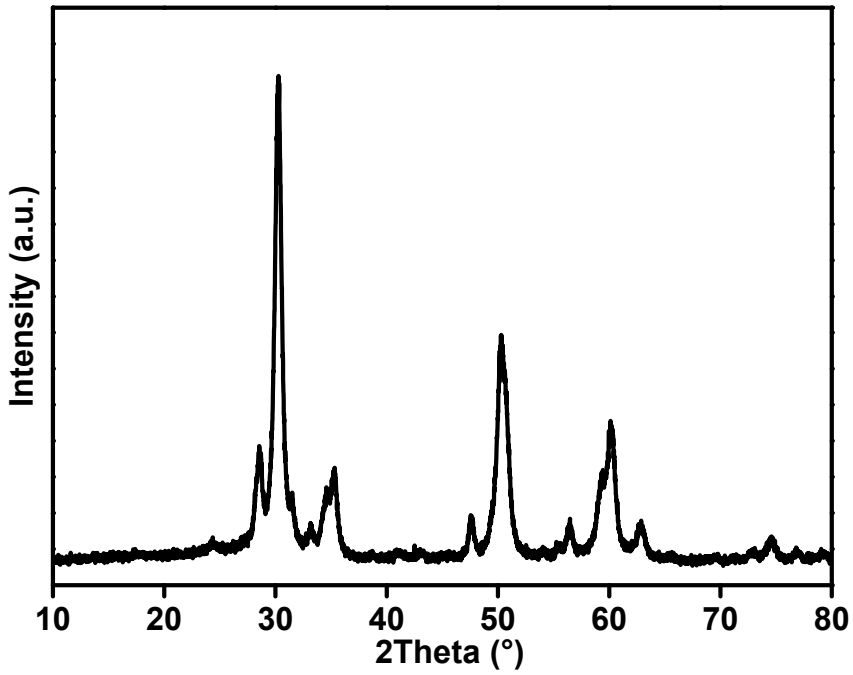

Figure S18. PXRD pattern of $Ce_xZr_{1-x}O_2$.

S18 GC chromatograms of CO and CO_2

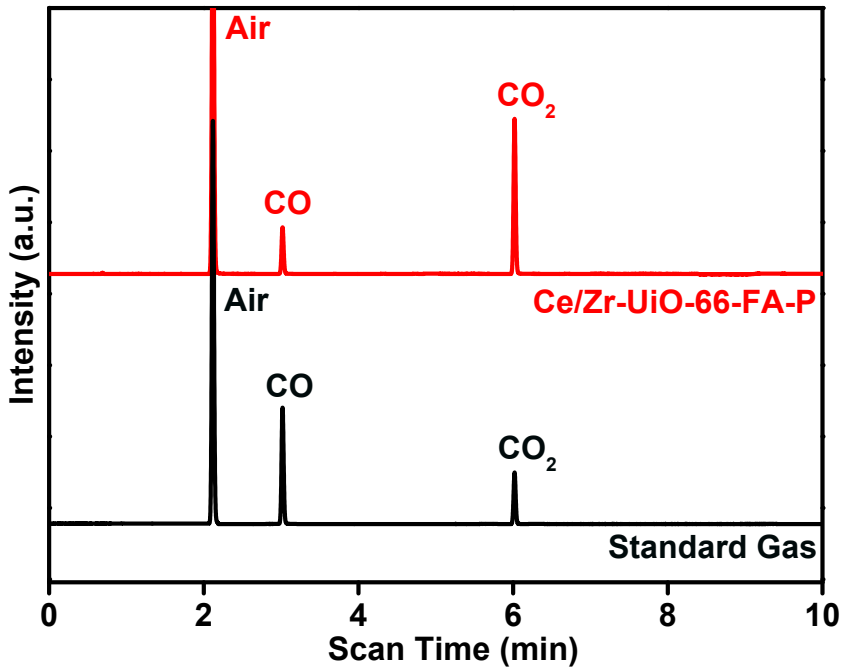

Figure S19. The GC chromatograms of CO and CO_2 from the reaction of HCB decomposition over Ce/Zr-UiO-66-FA-P catalyst at 250 °C for 1 h.

S19 Degradation efficiency of HCB over Metal Oxides and MOFs at 250 ℃

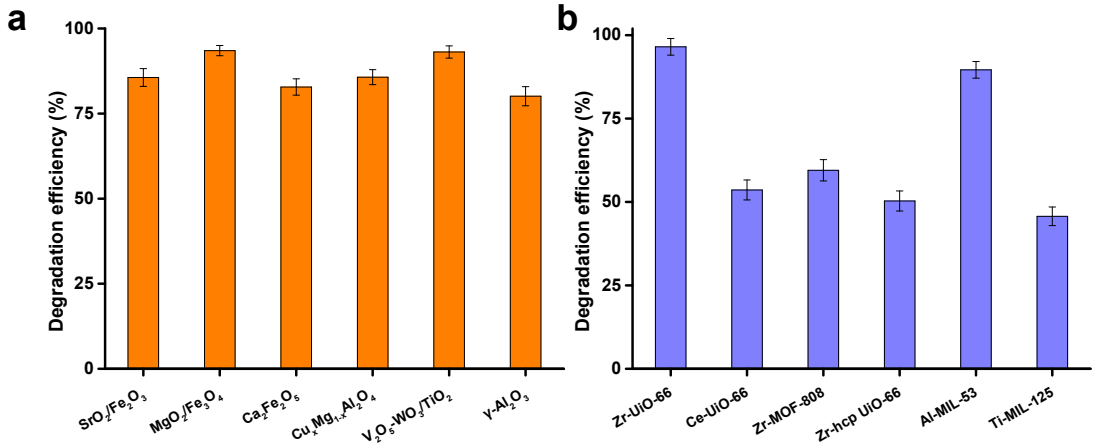

Figure S20. (a) Metal Oxides and (b) MOFs of the Degradation efficiency for HCB at 250 ℃ in 1h.

S20 PXRD patterns of the Zr-UiO-66, Ce-UiO-66, Zr-MOF-808, Zr-hcp UiO-66, Al-MIL-53 and Ti-MIL-125

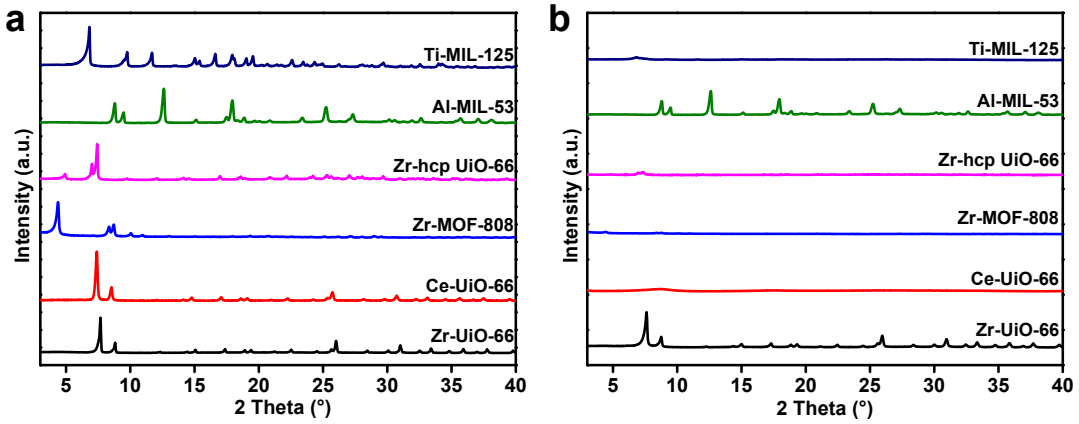

Figure S21. PXRD patterns of Zr-UiO-66, Ce-UiO-66, Zr-MOF-808, Zr-hcp UiO-66, Al-MIL-53, Ti-MIL-125 before catalytic degradation of HCB reaction (a) and after the reaction (b).

S21 Carbon distribution of the products over Metal Oxides and MOFs in the degradation of HCB at 250 ℃

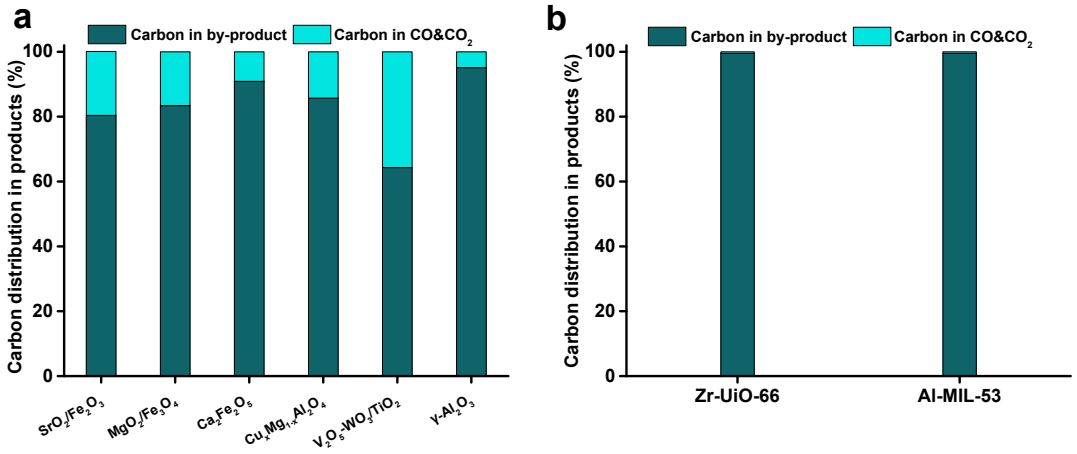

Figure S22. Carbon distribution of the products over (a) Metal Oxides and (b) MOFs for the catalytic degradation of HCB at 250 ℃ in 1h.

S22 Degradation efficiency of HCB and Carbon distribution of the products over Benchmarked acid/redox catalysts in the catalytic degradation of HCB.

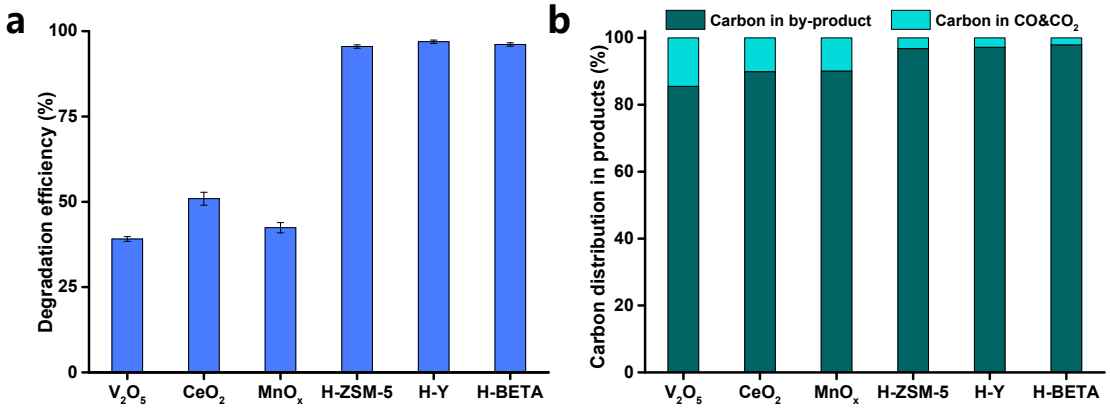

Figure S23. (a) Benchmarked acid/redox catalysts of the Degradation efficiency for HCB at 250 ℃ in 1h; (b) Carbon distribution of the products over Benchmarked acid/redox catalysts for the catalytic degradation of HCB at 250 ℃ in 1h.

S23 Characterization of catalysts after stability tests

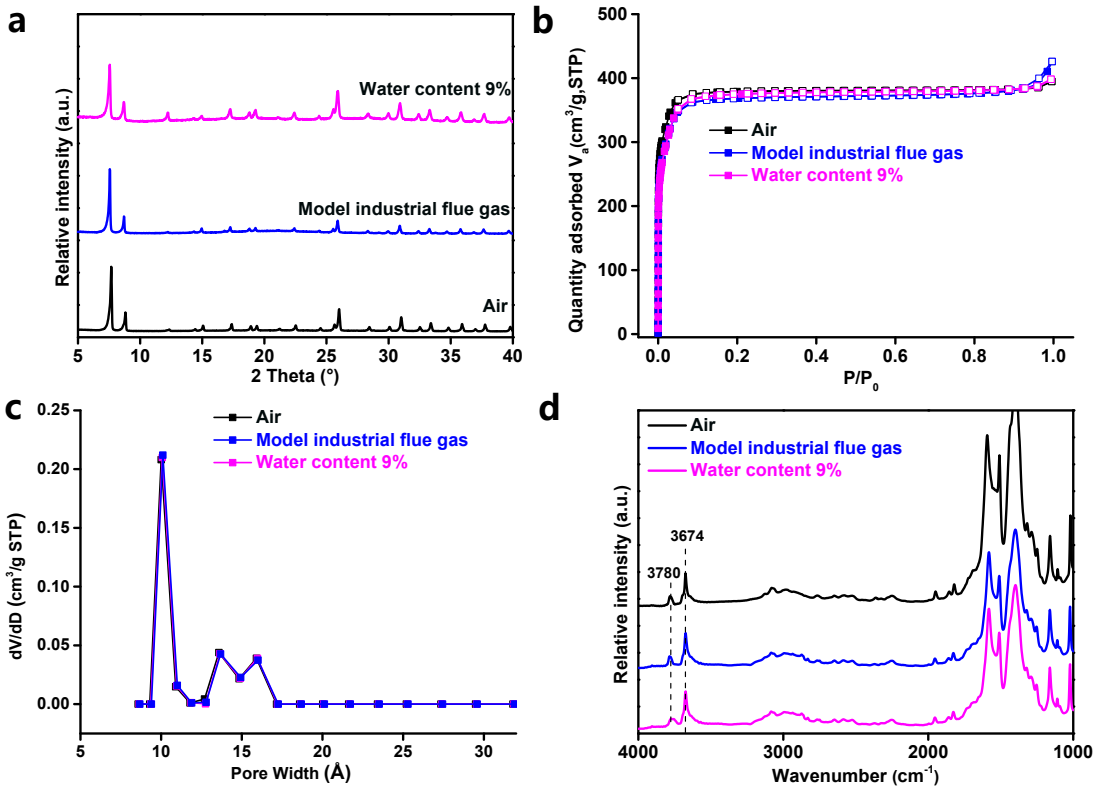

Figure S24. (a) PXRD pattern, (b) N2 isotherms, (c) Pore size distributions and (d) FT-IR spectra for Ce/Zr-UiO-66-FA-P after the catalyst stability tests.

Table S9. Number of defect sites per clusters and BET surface area of Ce/Zr-UiO-66-FA-P and Ce/Zr-UiO-66-FA-P after reaction.

Samples	Defect sites per clusters	BET surface area (m^2/g)	Pore Volume (cm^3/g)
Ce/Zr-UiO-66-FA-P in air	2.69	1347	0.65
Ce/Zr-UiO-66-FA-P in model industrial flus gas	2.76	1352	0.66
Ce/Zr-UiO-66-FA-P in water content 9%	2.73	1345	0.65

S24 Carbon distribution of the products for the catalytic degradation of HCB in the catalytic stability testing of Ce/Zr-UiO-66-FA-P

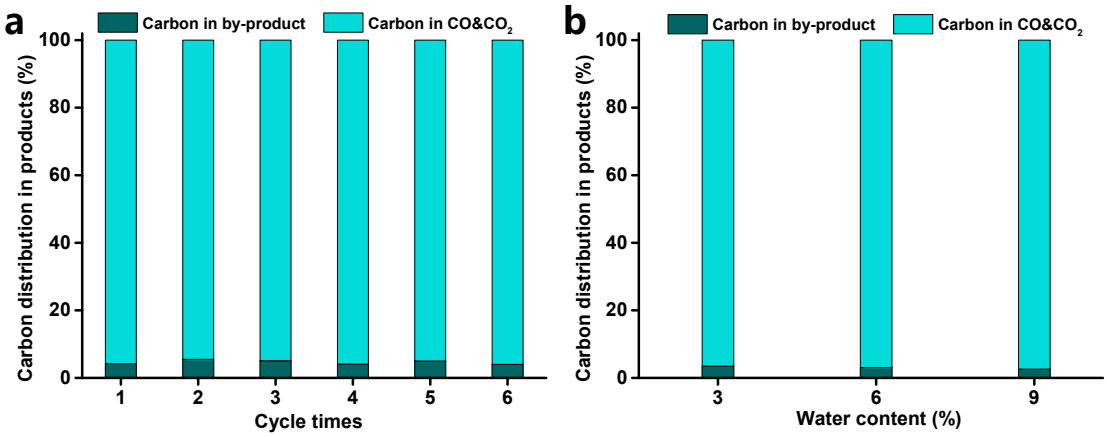

Figure S25. Carbon distribution of the products for the catalytic degradation of HCB in the catalytic stability testing of Ce/Zr-UiO-66-FA-P (a) Cycle reaction; (b) Different water content.

S25 Reusability of spent catalysts

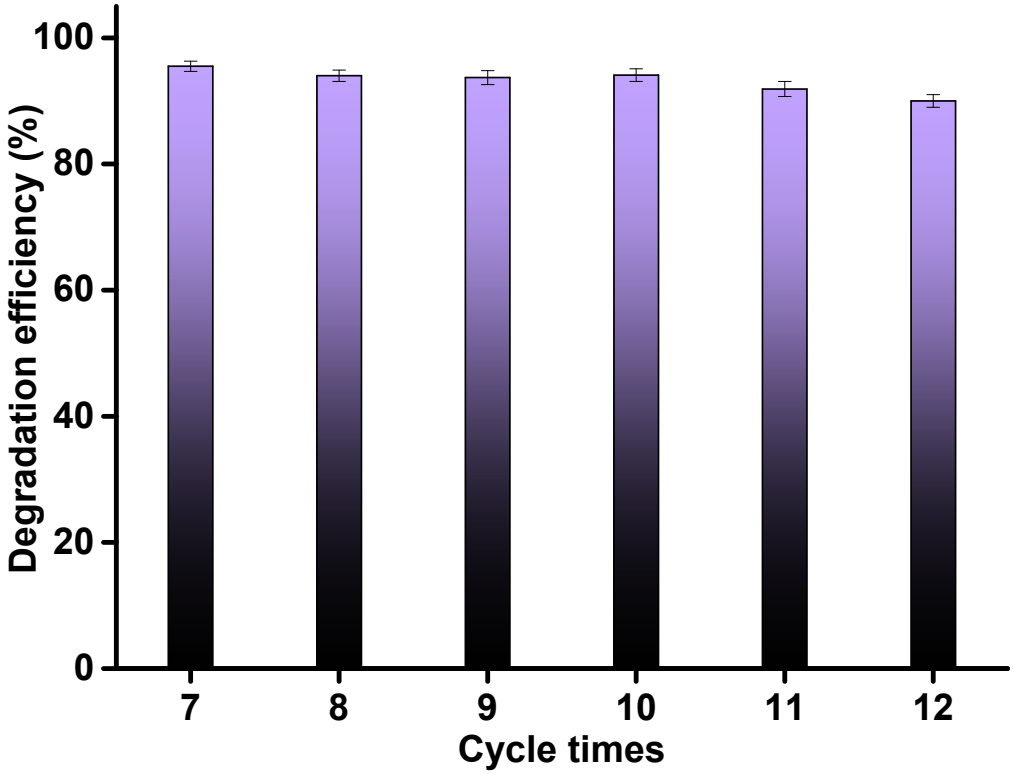

Figure S26. Catalytic degradation efficiency of HCB in model industrial flue gas over Ce/Zr-UiO-66-FA-P for six cycles reaction at 250 °C.

S26 Ce 3d XPS spectra of Ce/Zr-UiO-66-FA-P at 30 minutes during the catalytic degradation of HCB.

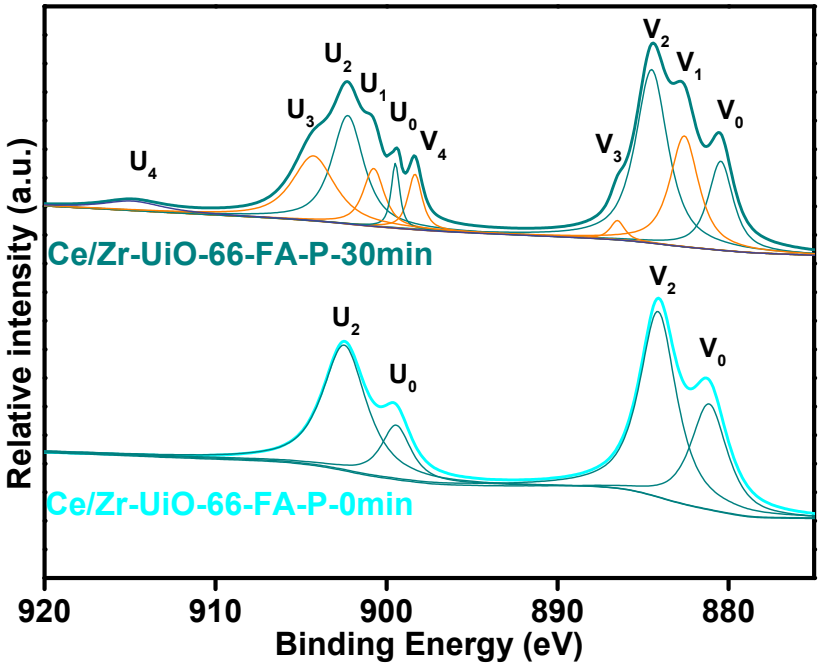

Figure S27. Ce 3d XPS spectra of Ce/Zr-UiO-66-FA-P at 0 minutes and 30 minutes during the catalytic degradation of HCB